Flyash radiative properties and effects on radiative heat transfer in coal-fired systems

D. G. GOODWIN† and M. MITCHNER

High Temperature Gasdynamics Laboratory, Department of Mechanical Engineering,
Stanford University, Stanford, CA 94305, U.S.A.

Abstract—The radiative properties of flyash polydispersions are calculated, allowing for realistic wavelength-dependent optical constants. Spectral absorption, scattering, and extinction efficiencies are presented, along with the spectral scattering asymmetry parameter. Wavelength-integrated Planck mean values are also given. The mean single-particle total emissivity ranges from approximately 0.05 to 0.15, depending on size distribution and temperature. The effects of magnetite particles in the ash on the radiative properties are discussed. The contribution of flyash to radiative heat transfer in coal combustion systems is examined, and for typical furnace conditions flyash is predicted to enhance the total emittance by approximately 20%.

1. INTRODUCTION

FLYASH is believed to make a significant contribution to radiative heat transfer in coal-fired systems. On the one hand, it is known from experience with pulverized coal boilers that the flame radiation characteristics are altered when the boilers are fired with coals with higher ash content [1]. Also, numerical studies of radiative heat transfer in coal-fired systems [2–9] have indicated that flyash may play an important role both by contributing to the radiative emission and by impeding the transport of flame radiation to the walls through scattering.

The predicted effects of flyash on heat transfer are, however, strongly dependent on the ash absorption and scattering coefficients used in the calculations. These coefficients depend in turn on the assumed complex refractive index $m = n - ik$ of the ash, as well as on the ash loading and size distribution. The studies to date have assumed that the optical constants n and k are independent of wavelength, with n taken in each case to be equal to 1.5 and with k values which have ranged from 0.005 to 0.05.

Consideration of the chemical makeup of flyash suggests that the assumption of wavelength-independent n and k is far from realistic. Flyash consists of a mixture of particles, the most abundant of which in most ashes are glassy spherical particles, consisting of impure aluminosilicate glasses. Various oxide mineral particles also occur in smaller amounts [5, 10]. The optical constants of aluminosilicate glasses, as well as of those of oxides such as SiO_2 and Al_2O_3,

are known to exhibit very large variations over the wavelength range of interest for heat transfer calculations (see, e.g. refs. [11, 12]). Usually for such materials, the imaginary part k of the refractive index varies by several orders of magnitude in the wavelength range $\lambda = 1$–$10\ \mu$m.

In this paper, we examine the effects of flyash on radiative heat transfer, allowing for realistic wavelength-dependent optical constants. The analysis shows that the highly non-grey character of flyash results in predictions regarding the flyash contribution to heat transfer which differ significantly from those of previous studies.

2. FLYASH MODEL

2.1. *Size distribution*

Two different size distributions were used in the present calculations, representing a fine and a coarse ash, respectively. Both distributions were assumed to be log-normal in form, so that the fraction of particles $f(D)$ with diameters between D and $D + dD$ is

$$f(D) = \frac{1}{\sqrt{(2\pi)}D\sigma_u} \exp\left[-(\ln D - \bar{u})^2/2\sigma_u^2\right] \quad (1)$$

where $\bar{u}$ and σ_u are measures of location and width, respectively. The parameters $\bar{u}$ and σ_u for the two distributions used here are given in Table 1, along with the mass median diameter (MMD), r.m.s. diameter (D_{20}), mass mean diameter (D_{30}), and Sauter mean diameter (D_{32}) for these distributions. The mean diameters D_{nm} are defined by

$$(D_{nm})^{n-m} = \langle D^n \rangle / \langle D^m \rangle \quad (2)$$

where the angular brackets denote averaging over the size distribution. ($\langle F \rangle = \int_0^\infty F(D)f(D)\,dD$.)

Size distribution A was obtained from measure-

† Present address: Department of Mechanical Engineering, California Institute of Technology 104-44, Pasadena, CA 91125, U.S.A.

NOMENCLATURE

A_p projected area per unit mass
C_2 second radiation constant
D particle diameter
D_{nm} mean particle diameter
$e_{\lambda b}$ spectral blackbody emissive power
$f(D)$ size distribution function
g_λ asymmetry parameter
$\bar{g}_\lambda$ asymmetry parameter for polydispersion
k imaginary part of refractive index
K_λ absorption, scattering, or extinction coefficient for particle dispersion
$K'_{\lambda s}$ effective isotropic scattering coefficient
$K_{\lambda a, gas}$ gas absorption coefficient
L pathlength used to calculate τ_g
m complex refractive index
M particle mass loading
n real part of refractive index
$P_\lambda(\mu)$ scattering phase function
Q_λ efficiency computed from Lorenz–Mie expressions
$\bar{Q}_\lambda$ size-distribution-averaged efficiency
$\bar{\bar{Q}}_\lambda$ size-and-composition-averaged efficiency
T temperature
T_{max} maximum temperature for which k data available

T_R temperature of incident blackbody radiation
$\bar{u}$ parameter in log-normal distribution function
x size parameter.

Greek symbols
ε slab total hemispherical emittance
ε_λ slab spectral hemispherical emittance
$\bar{\varepsilon}_p$ mean single-particle total emissivity
λ wavelength
λ_c Christiansen wavelength, $n(\lambda_c) = 1.0$
μ cosine of scattering angle
ρ density
σ Stefan–Boltzmann constant
σ_u parameter in log-normal distribution function
τ slab diffuse transmittance for blackbody radiation
τ_λ slab spectral diffuse transmittance
τ_g gas narrow-band transmittance.

Subscripts
a   absorption
e   extinction
p   Planck mean quantity
s   scattering
λ wavelength-dependent quantity.

ments in this laboratory on flyash collected at a middle-field location of an electrical power-plant electrostatic precipitator [13]. This ash probably contained fewer of the larger particles than would be present in a furnace, since the larger particles are collected preferentially at the precipitator entrance. Size distribution B is based on the coarsest distribution used by Gupta et al. [8]. The parameters $\bar{u}$ and σ_u were chosen to match the MMD and the r.m.s. diameter given in ref. [8].

2.2. Optical constants

The optical constants used in the present calculations are shown in Fig. 1. These values are taken from Goodwin [14], in which the optical constants were measured for homogeneous bulk samples with compositions similar to those of flyash particles. Measurements of k were also made at a series of elevated temperatures, and the highest-temperature k

values are shown along with the room temperature values in Fig. 1. The strong wavelength dependence of the optical constants is apparent.

The optical constants used for most of the calculations in this paper are those shown in Fig. 1(b), which were measured for a sample with a composition of 52.05% SiO_2, 26.80% Al_2O_3, 15.68% CaO, and 5.47% Fe_2O_3, on a weight percent basis, which was in a fully reduced state (all Fe in the form Fe^{2+}). This composition corresponds to typical values for the mean composition of a sub-bituminous ash [15].

The optical constants shown in Fig. 1(a) are for a sample of similar composition to that of Fig. 1(b), except that it is essentially iron-free (56.16% SiO_2, 27.54% Al_2O_3, 16.26% CaO, and 0.04% Fe_2O_3). These optical constants were used for the glassy, iron-free ash particles considered in Section 4.

The temperature dependence of k was included in the calculations to the extent possible, although due to limited data this could not be done in a completely consistent manner. For temperatures up to the highest temperature T_{max} at which measurements were made in ref. [14], the measured high-temperature k values were used for the wavelength range 1–7.8 μm. Outside this wavelength range, no high-temperature k data were available, and thus the room temperature k values were used. This is a reasonable approximation,

Table 1. Log-normal size distribution parameters

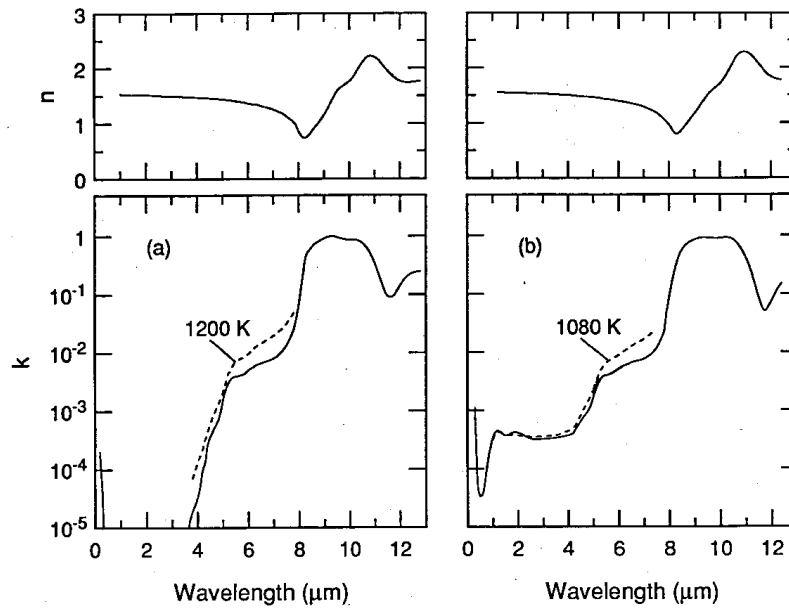|	$\bar{u}$	σ_u	MMD (μm)	D_{20} (μm)	D_{30} (μm)	D_{32} (μm)
A	−0.214	0.747	4.3	1.41	1.86	3.25
B	0.35	0.971	24.0	3.65	5.8	14.9

FIG. 1. Optical constants used in the present calculations, taken from ref. [14]. The values shown in (a) were measured for an iron-free sample, and those shown in (b) were measured for a sample with 5.47% Fe_2O_3. The solid curves are room temperature values, and the dashed curves show the highest-temperature measured k values.

since the large k values which occur at longer wavelengths result from fundamental vibrational absorption, which (at least according to simplified theories) should be independent of temperature [16].

For temperatures higher than T_{max}, the k values at T_{max} were used in the wavelength range 1–4.1 μm, since the temperature dependence in this wavelength region is in any case small. For the wavelength range 4.1–7.8 μm, the value of k was extrapolated from the measured value at T_{max} using the approximate overtone-absorption scaling law

$$k(T) \propto 1 + \frac{2}{\exp{(C_2/2\lambda T)} - 1} \tag{3}$$

where $C_2 = 14388$ μm K. The temperature dependence of k measured in ref. [14] was shown to be well described by equation (3) in this wavelength range, for temperatures from room temperature to T_{max}. The fact that equation (3) is based on theoretically sound considerations and contains no adjustable parameters (i.e. it is not a fit to the experimental data) makes it plausible to assume that it applies at still higher temperatures. Extrapolating k to 1800 K by means of equation (3) from measured values at 1080 K results in an increase by a factor of 1.48 at 4.1 μm, and by 1.61 at 7.8 μm.

The temperature dependence of n, which is expected to be small, was not measured in ref. [14], and thus the room temperature n values were used in the calculations. For oxides similar to flyash, typical values for dn/dT are 10^{-5} K^{-1} away from strong resonances [17], which would give a change in n of less than 0.01 at flame temperatures over the room temperature values. In the long-wavelength vibrational resonance region, n is also expected to be relatively temperature

independent, since, like k, its value is determined by fundamental vibrational processes [16].

3. SPECTRAL RADIATIVE PROPERTIES FOR FLYASH POLYDISPERSIONS

The properties of a flyash polydispersion needed for radiative heat transfer calculations are the spectral absorption coefficient $K_{\lambda a}$, the spectral scattering coefficient $K_{\lambda s}$, and the scattering phase function $P_\lambda(\mu)$, where μ is the cosine of the scattering angle. Often, however, the anisotropic nature of the scattering is treated approximately, using scaled parameter values for the isotropic problem [8, 18]. In this case, one needs only the asymmetry parameter g_λ of the phase function, instead of the phase function itself, where g_λ is given by

$$g_\lambda = \frac{1}{2} \int_{-1}^{1} P_\lambda(\mu)\mu \, d\mu. \tag{4}$$

If the ash particles all have the same composition, then the absorption coefficient of the ash polydispersion may be written as

$$K_{\lambda a} = MA_p \bar{Q}_{\lambda a} \tag{5}$$

where M is the mass loading of particulates (g m^{-3}), A_p the projected area of the particles per unit mass (m^2 g^{-1}), and $\bar{Q}_{\lambda a}$ the size-distribution-averaged absorption efficiency. If the particles are assumed to be spherical (generally a good assumption for flyash), then A_p is given by

$$A_p = \frac{3}{2}(\rho D_{32})^{-1} \tag{6}$$

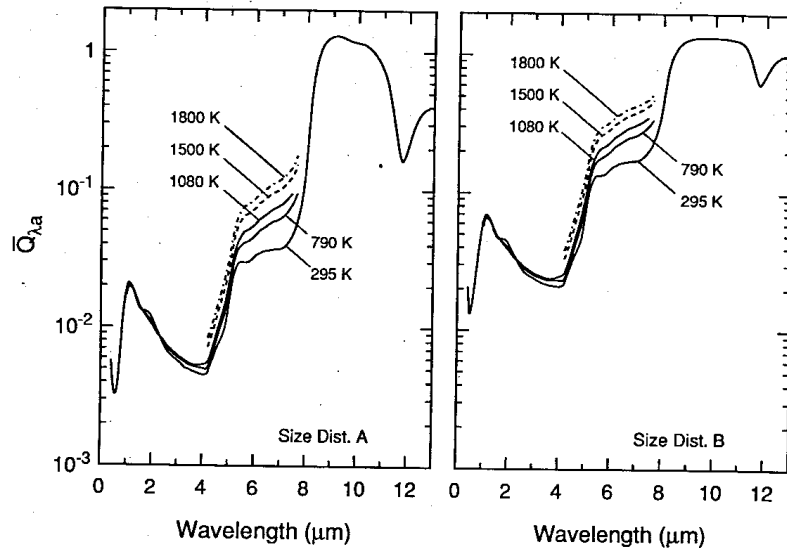where ρ is the material density (g m^{-3}).

FIG. 2. Mean spectral absorption efficiency. Results computed using extrapolated k values are shown dashed.

The average absorption efficiency $\bar{Q}_{\lambda a}$ is given by

$$\bar{Q}_{\lambda a} = \langle D^2 Q_{\lambda a} \rangle / \langle D^2 \rangle \qquad (7)$$

where $Q_{\lambda a}$ is the absorption efficiency computed from the Lorenz–Mie expressions as a function of the size parameter $x = \pi D / \lambda$ and the complex refractive index $m(\lambda)$.

Equivalent expressions for the scattering coefficient $K_{\lambda s}$ or for the extinction coefficient $K_{\lambda e}$ (defined as $K_{\lambda e} = K_{\lambda s} + K_{\lambda a}$) are obtained by replacing the subscript a in equations (5) and (7) with the subscript s or e, respectively.

The asymmetry parameter $\bar{g}_\lambda$ for the scattering phase function of the polydispersion is given by

$$\bar{g}_\lambda = \frac{\langle g_\lambda Q_{\lambda s} D^2 \rangle}{\langle Q_{\lambda s} D^2 \rangle} \qquad (8)$$

where g_λ and $Q_{\lambda s}$ are computed from the Lorenz–Mie expressions as functions of x and $m(\lambda)$.

The spectral mean absorption, scattering, and extinction efficiencies and the spectral mean asymmetry parameter were computed for a model ash dispersion, subject to the assumptions discussed above.

(1) The particles are all spherical and internally homogeneous. The small fraction of other particle morphologies (e.g. hollow cenospheres, angular crystallites) is ignored.

(2) The particle distribution is log-normal, given by either distribution A or B of Table 1.

(3) The particles are all identical in composition, and have the optical constants shown in Fig. 1(b).

The computed spectral mean absorption efficiency $\bar{Q}_{\lambda a}$ is shown in Fig. 2. The features seen in the absorption efficiency spectrum all have parallels in the spectrum of the imaginary part of the refractive index (cf. Fig. 1(b)). No additional Lorenz–Mie structure is apparent, indicating that the fine ripple structure exhibited by the Lorenz–Mie solutions for a single

particle is completely washed out by integrating over the size distribution. The particles are weakly absorbing at short wavelengths ($\lambda < 5 \ \mu m$), with $\bar{Q}_{\lambda a} < 10\%$ in this wavelength range for both size distributions. For size distribution A, the absorption efficiency drops to below 1% from 2 μm to nearly 5 μm. At longer wavelengths, the ash becomes highly absorptive, with $\bar{Q}_{\lambda a}$ rising above 1.0.

Comparing the results for size distributions A and B indicates the effects of particle size on the absorption efficiency. At wavelengths where the particles are weakly absorbing, the mean absorption efficiency scales approximately with D_{32}. This scaling follows from equation (7), since $Q_{\lambda a}$ for a single particle scales linearly with D (neglecting ripple structure) when $kD/\lambda \ll 1$ and $n - 1 \ll 1$. Since the absorption coefficient is proportional to $\bar{Q}_{\lambda a}/D_{32}$, it is relatively independent of the size distribution as long as these conditions are satisfied.

At longer wavelengths, where the particles are strongly absorbing, $\bar{Q}_{\lambda a}$ is similar for the two size distributions. Thus, in this wavelength range, the absorption coefficient scales approximately inversely with D_{32}.

The effects of temperature (through the temperature dependence of k) on the mean absorption efficiency are seen to be significant in the 5–8 μm range. For size distribution A, the mean absorption efficiency at 7 μm rises by more than a factor of 3 in going from room temperature to 1800 K. For size distribution B in this wavelength range, $\bar{Q}_{\lambda a}$ reaches values of 30–50% at 1800 K. For wavelengths below about 5 μm, the effects of temperature are relatively small, since k has a small temperature dependence in this region.

The mean scattering and extinction efficiencies are shown in Fig. 3. For size distribution A, both efficiencies peak near 1.5 μm, and decrease nearly linearly with increasing wavelength up to the
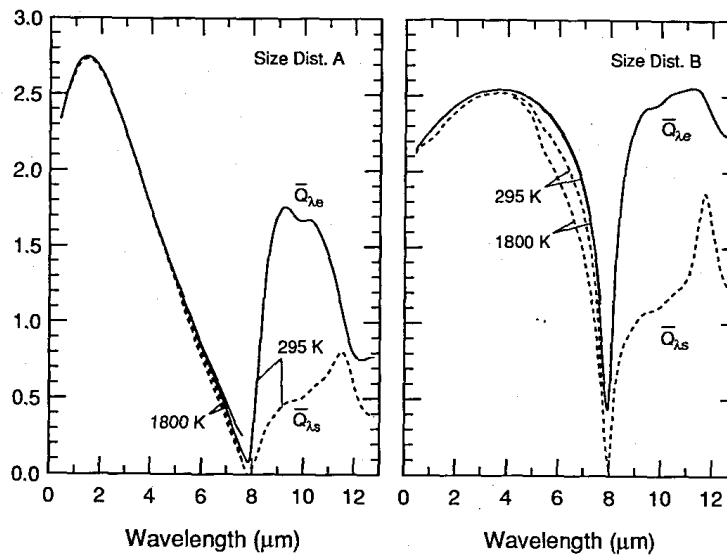
FIG. 3. Mean spectral scattering efficiency (dashed curve) and extinction efficiency (solid curve).

Christiansen wavelength (defined by $n(\lambda_c) = 1.0$) at 7.9 μm. At this point, the scattering efficiency is very nearly zero. The peak in $\bar{Q}_{\lambda s}$ and $\bar{Q}_{\lambda e}$ is broader and shifted to longer wavelengths for size distribution B, and thus the decrease in the efficiencies near 7.9 μm occurs over a much narrower wavelength interval than it does for distribution A. Beyond 8 μm, the scattering and extinction efficiencies differ significantly from one another, since the absorption efficiency is large in this wavelength region. The effects of temperature on the scattering and extinction efficiencies are seen to be relatively minor. It should be noted that the strong drop in $\bar{Q}_{\lambda s}$ and $\bar{Q}_{\lambda e}$ near 8 μm was not predicted in previous studies, since in these n was assumed to be constant and greater than 1.0.

The results for the mean asymmetry parameter for the two size distributions are shown in Fig. 4. The results show, as expected, that scattering by the ash particles is highly forward directed ($\bar{g}_\lambda > 0$), with scat-

tering by the coarser ash B more forward directed than that by the finer ash A. Temperature is seen to have little effect on $\bar{g}_\lambda$.

4. EFFECTS DUE TO MAGNETITE PARTICLES

In the previous section, the ash was assumed to consist only of glassy particles, which were taken to all have the same composition. In reality, however, flyash contains a small admixture of non-glassy particles, some of which appear opaque under an optical microscope [19]. Some of the opaque particles are carried-over char or soot, but others are iron oxide particles, in the form of either hematite (Fe_2O_3) or magnetite (Fe_3O_4). The iron oxide particles generally have a coarser size distribution than the glassy particles [19], and may contain a significant fraction of the total iron content of the ash [20].

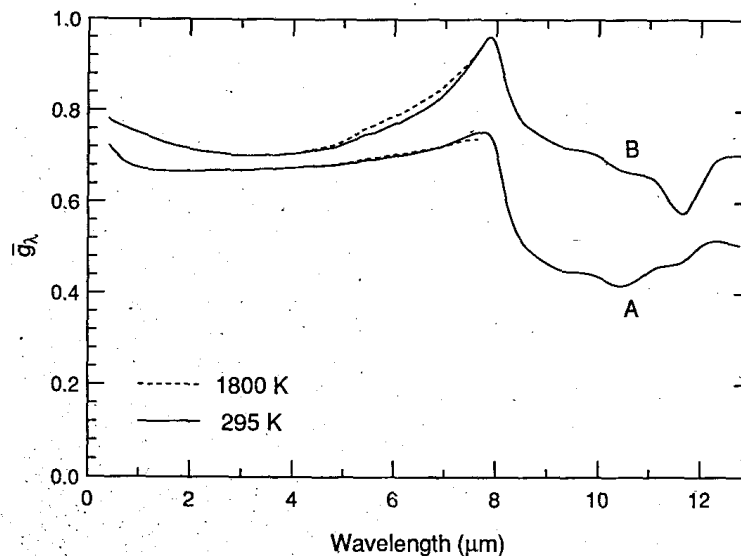The possible effects of iron oxide particles on the

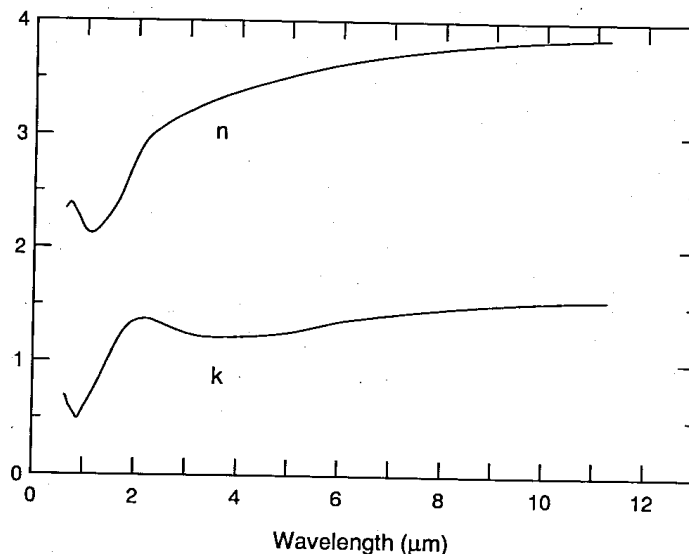FIG. 4. Mean spectral asymmetry parameter for size distributions A and B.

FIG. 5. The optical constants of magnetite (Fe$_3$O$_4$) used for the present calculations. These values were computed from data given by Schlegel et al. [22].

ash radiative properties depend on which form the particles take. Hematite particles, although visually deep red, are essentially transparent in the infra-red, since k is less than 10^{-6} at infra-red wavelengths [21]. Magnetite, however, is a black mineral which remains highly absorbing ($k \approx 1$) throughout the infra-red.

The effects of magnetite particles on the ash radiative properties were investigated by considering the limiting case in which all of the iron in the ash occurs as magnetite (no hematite particles and no Fe in the glassy particles). The total iron content was held the same as that for the homogeneous glassy ash of the previous section, namely, 5.47% by weight expressed as Fe$_2$O$_3$. Accounting for the different molecular weights of Fe$_2$O$_3$ and Fe$_3$O$_4$, this corresponds to an ash with 5.3% magnetite by weight, so the ash for the calculations here is taken to consist of:

(a) 5.3% by wt. magnetite particles;
(b) 94.7% by wt. glassy Fe-free particles.

The optical constants for the glassy particles are taken to be those shown in Fig. 1(a). The optical constants for magnetite were calculated from the room temperature infra-red dielectric function data of Schlegel et al. [22] and are shown in Fig. 5. The radiative properties calculated using these optical constants for a magnetite polydispersion distributed according to either size distribution A or B are shown in Fig. 6.

For a mixture of different particle types, the absorption coefficient may be obtained by summing equation (5) over each particle class. Alternatively, a mean absorption efficiency for the mixture may be defined by generalizing equation (5) as

$$K_{\lambda a} = MA_p \bar{\bar{Q}}_{\lambda a} \qquad (9)$$

where $\bar{\bar{Q}}_{\lambda a}$ is the composition-averaged efficiency, weighted by the projected area of each composition class

$$\bar{\bar{Q}}_{\lambda a} = \frac{\Sigma_i A_{p,i} \bar{Q}_{\lambda a,i}}{A_p}. \qquad (10)$$

The composition-averaged mean absorption efficiency for the two-component glass/magnetite ash is shown in Fig. 7, for a temperature of 1500 K. The absorption efficiency computed previously for the single-component ash is also shown for comparison. The high-temperature k values for the glassy particles at 1500 K (scaled using equation (3) from 1200 K) were used for $\lambda < 7.6$ μm, and the room temperature k values were used for $\lambda > 8.1$ μm. The computed values of $\bar{\bar{Q}}_{\lambda a}$ are joined with a smooth curve between 7.6 and 8.1 μm.

The absorption efficiencies for the two cases are seen to differ primarily in the short wavelength region, where the glassy particles are weakly absorbing. Whether the two-component ash has a higher absorption efficiency in this wavelength region depends on the relative size distributions of the magnetite and glassy particles. If both phases are distributed according to size distribution A (curve (a) in Fig. 7), the magnetite-bearing ash is significantly more absorbing than the homogeneous ash for $\lambda < 5$ μm. Nevertheless, the mean absorption efficiency in the short wavelength region is still only 3% for the magnetite-bearing ash.

If the magnetite particles are distributed according to distribution B (curves (b) and (c)), then the magnetite-bearing ash is actually less absorbing at short wavelengths than the homogeneous ash, for either size distribution for the glassy particles. This is probably the more realistic assumption, since the iron oxide particles are known to be distributed more coarsely than the glassy particles in flyash [19].

These results suggest that the presence of iron oxide particles in the ash will not increase the absorption efficiency significantly beyond that calculated assuming a homogeneous iron distribution in the
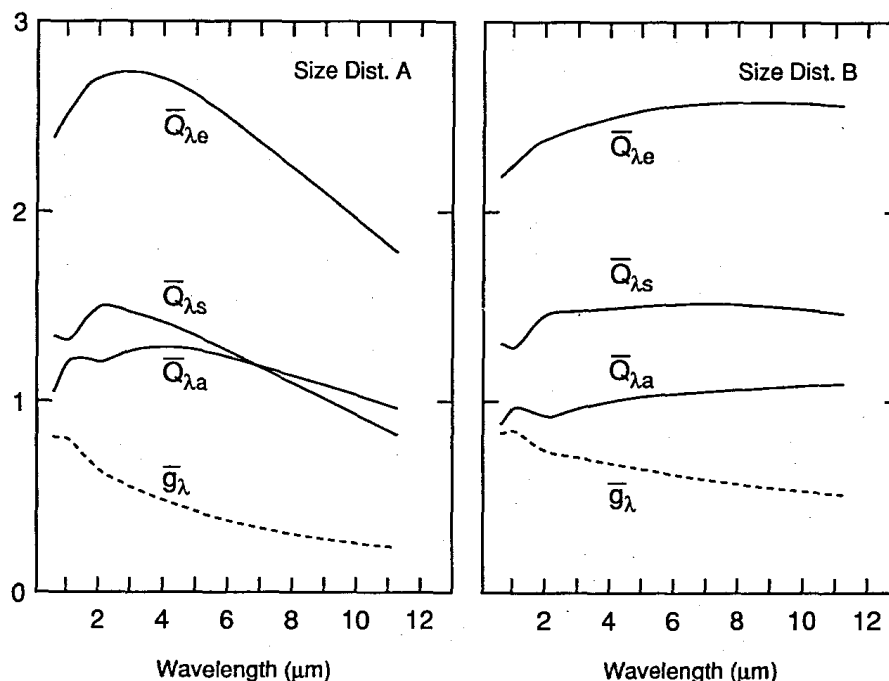
FIG. 6. Mean efficiencies (absorption, scattering, and extinction) and mean asymmetry parameter for a magnetite polydispersion with size distribution A or B.

glassy phase, and may actually decrease it. The value of the mean absorption efficiency in the short wavelength region ($\lambda < 4 \, \mu m$) will be of the order of a few percent (at most), for any reasonable assumptions regarding the size or iron distribution of the ash dispersion.

Similar calculations were carried out for the scattering and extinction efficiencies, and for the asymmetry parameter. However, these were found to differ only negligibly for the magnetite-bearing ash from the previously computed values for the homogeneous ash.

5. WAVELENGTH INTEGRATED PROPERTIES

It is not always possible to perform radiative heat transfer calculations on a spectral level, either due to the prohibitive computation time required or because the computation scheme employed (e.g. the zone method) is formulated in terms of total properties. In such cases, wavelength-integrated absorption, scattering, and extinction coefficients are required. These may be computed from appropriately defined mean efficiencies, using equation (5).
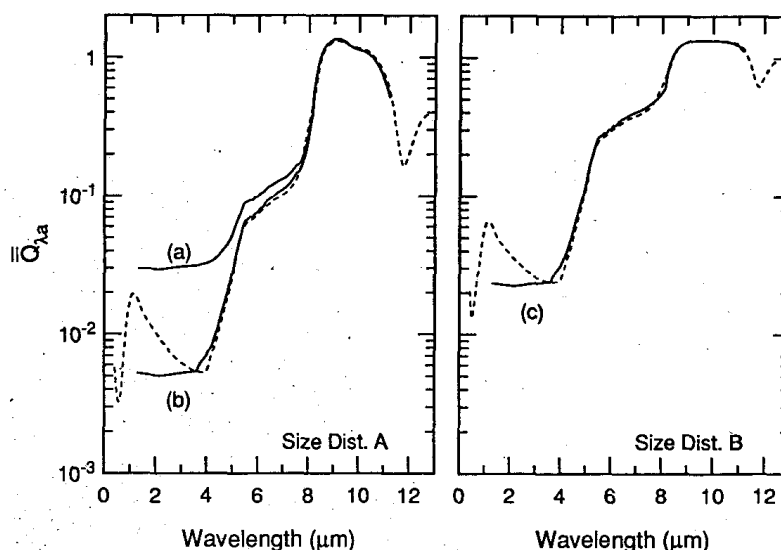
FIG. 7. The effect of magnetite particles on the mean absorption efficiency, for $T = 1500$ K. The two plots are for distributions A and B, respectively, for the glassy particles. Curve (a): magnetite particles distributed according to distribution A. Curves (b) and (c): magnetite particles distributed according to distribution B. The dashed curves show the values for the homogeneous ash from Fig. 2.

The Planck mean absorption efficiency, useful when the medium is optically thin, is defined as

$$\bar{Q}_{pa} = \frac{1}{\sigma T_R^4} \int_0^\infty \bar{Q}_{\lambda a}(T) e_{\lambda b}(T_R) \, d\lambda \qquad (11)$$

where $e_{\lambda b}(T_R)$ is the spectral blackbody emissive power at the incident radiation temperature T_R. Similar expressions apply for the Planck mean scattering and extinction efficiencies. Using Kirchhoff's law, it is easily shown that $\bar{Q}_{pa}$ evaluated for $T = T_R$ is equal to the average single-particle total emissivity $\bar{\varepsilon}_p$, defined such that the power radiated per unit volume by the ash dispersion is $4MA_p\bar{\varepsilon}_p\sigma T^4$.

A Planck mean asymmetry parameter may also be defined, which is given by

$$\bar{g}_p = \frac{1}{\sigma T_R^4 \bar{Q}_{ps}} \int_0^\infty \bar{Q}_{\lambda s}(T) \bar{g}_\lambda(T) e_{\lambda b}(T_R) \, d\lambda. \quad (12)$$

The mean single-particle emissivity, the Planck mean extinction efficiency, and the Planck mean asymmetry parameter were calculated for the homogeneous ash using the spectral data shown in Figs. 2–4, for the temperature range 1200–1800 K. For simplicity, the calculations of $\bar{Q}_{pe}$ and $\bar{g}_p$ were carried out for the case $T = T_R$. Since the spectral quantities $\bar{Q}_{\lambda e}$ and $\bar{g}_\lambda$ are nearly independent of T, this simplification does not affect the results significantly.

The wavelength integrals in equations (11) and (12) were evaluated numerically for the wavelength range from 0.4 to 12.8 μm. The fraction of the total blackbody flux contained in this wavelength range is 0.971 at 1200 K, and 0.990 at 1800 K, with the excluded fraction primarily on the long wavelength side. For $\bar{Q}_{pe}$ and $\bar{g}_p$, the computed values were normalized by the blackbody fraction within the integration range, resulting in an overestimate of at most 3% at 1200 K and 1% at 1800 K. For the absorption efficiency calculations, $\bar{Q}_{\lambda a}$ was assumed to have a constant value for wavelengths $\lambda > 12.8$ μm.

The results for $\bar{\varepsilon}_p$, $\bar{Q}_{pe}$, and $\bar{g}_p$ are shown in Fig. 8, for both size distributions A and B. The shaded regions in the emissivity plot indicate the uncertainty in $\bar{\varepsilon}_p$ resulting from assuming values for $\bar{Q}_{\lambda a}$ for $\lambda > 12.8$ μm ranging from 0.4 to 0.8.

The single-particle emissivity varies from about 5% to about 15%, depending on temperature and size distribution. The value decreases with increasing temperature, due to the stronger weighting of short wavelengths, where the spectral absorption efficiency is low. Due to the large value of $\bar{Q}_{\lambda a}$ at long wavelengths, approximately 50% of the value of $\bar{\varepsilon}_p$ is contributed by the wavelength region $\lambda > 9$ μm, even though the fraction of the total blackbody flux in this long-wavelength region is small at these temperatures. The decrease of $\bar{\varepsilon}_p$ with temperature is solely due to the temperature dependence of the blackbody weighting function, and is not affected significantly by our assumptions regarding the temperature dependence of the optical constants: if room temperature optical
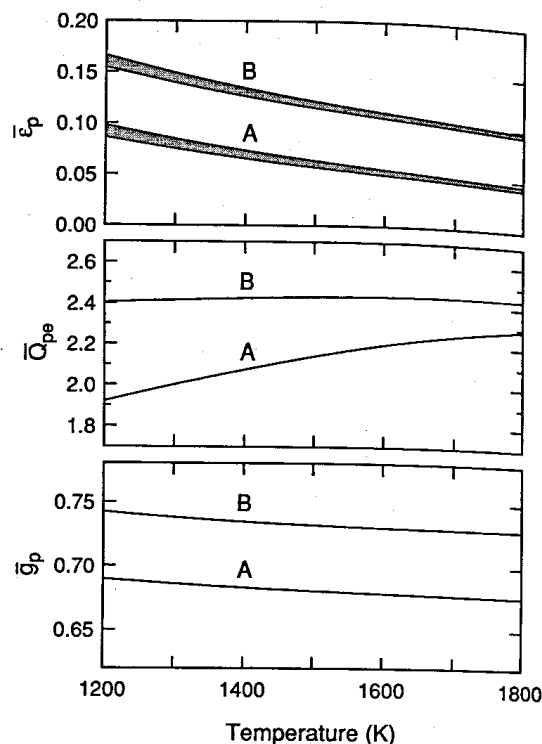

FIG. 8. Mean single-particle total emissivity, Planck mean extinction efficiency, and Planck mean asymmetry parameter for the two size distributions A and B.

constants had been used for all temperatures, the decrease in $\bar{\varepsilon}_p$ with temperature would have been still larger.

The value of $\bar{\varepsilon}_p$ is greater for the coarser size distribution, as expected, but the increase is not in proportion to the increase in D_{32}. Thus, the emissive power of the ash per unit mass (proportional to $A_p\bar{\varepsilon}_p$) is greater for size distribution A than for B.

It should be noted that the temperature dependence of $\bar{\varepsilon}_p$ computed here is opposite to that predicted in previous studies, which all assumed wavelength-independent optical constants [6, 9, 23]. These studies all showed ε_p increasing with temperature. Such a temperature dependence always results if wavelength-independent optical constants are assumed, since the spectral absorption efficiency is in this case a decreasing function of wavelength.

The Planck mean extinction efficiency increases with temperature for size distribution A (approximately 20% over this temperature range), but is nearly independent of temperature for size distribution B. The Planck mean asymmetry parameter decreases slightly with increasing temperature, though the decrease is so small that for most purposes the temperature dependence of $\bar{g}_p$ could be neglected.

6. THE EFFECTS OF FLYASH ON RADIATIVE HEAT TRANSFER

The spectral radiative properties computed above are used here to investigate the effects of flyash on radiative heat transfer for conditions typical of coal-

Table 2. Model problem parameters

Temperature	1500 K
P_{H_2O}	0.08 atm
P_{CO_2}	0.145 atm
Slab thickness	3 m
Ash mass loading	6.5 g m^{-3}

fired furnaces. Our primary interest in carrying out these calculations is to examine the effects on heat transfer of the strongly non-grey nature of the radiative properties of flyash. Consequently, we confine our attention to a geometrically simple model problem.

The problem to be examined is an isothermal slab with transparent boundaries, which contains water vapor, carbon dioxide, and flyash. (No account is taken of carbon in the ash.) The dimensions of the slab, the temperature, the partial pressures of the gas species, and the ash loading are chosen to approximate typical values for a pulverized-coal furnace burning a high-ash coal, and are based on values suggested by Wall et al. [5]. The parameter values are given in Table 2.

The spectral hemispherical emittance ε_λ and the spectral diffuse transmittance τ_λ of the slab were computed by solving the equation of radiative transfer exactly using the Case Normal Modes technique [24]. The solution for isotropic scattering was used, with a scaled scattering coefficient to account for anisotropic scattering. The effective isotropic scattering coefficient $K'_{\lambda s}$ was computed as

$$K'_{\lambda s} = (1 - \bar{g}_\lambda)K_{\lambda s}. \qquad (13)$$

This scaling was found by Gupta et al. [8] to give the best results of the several schemes they investigated, and gave errors in the slab hemispherical properties of approximately 2%.

The spectral absorption coefficients of water vapor and carbon dioxide were calculated using the single line group (SLG) model of Ludwig et al. [25]. To calculate the collision broadening coefficient, the background gas was assumed to be nitrogen. An absorption coefficient for the gas was computed as

$$K_{\lambda a,gas} = -\ln (\tau_g)/L \qquad (14)$$

where τ_g is the narrow-band transmittance of the gas mixture calculated from the SLG model, and L the pathlength used to calculate τ_g. Due to the effects of averaging over line structure in the narrow band model, the transmittance τ_g is non-exponential, and thus $K_{\lambda a,gas}$ is pathlength dependent. However, for combustion temperatures and pressures the pathlength dependence is small, since the lines tend to be broad and overlapping, in which case the narrow-band transmittance deviates only slightly from the exponential form. In the present calculations, the gas absorption coefficient is evaluated with L equal to twice the slab thickness, which is the geometric mean beam length in the optically-thin, non-scattering limit.
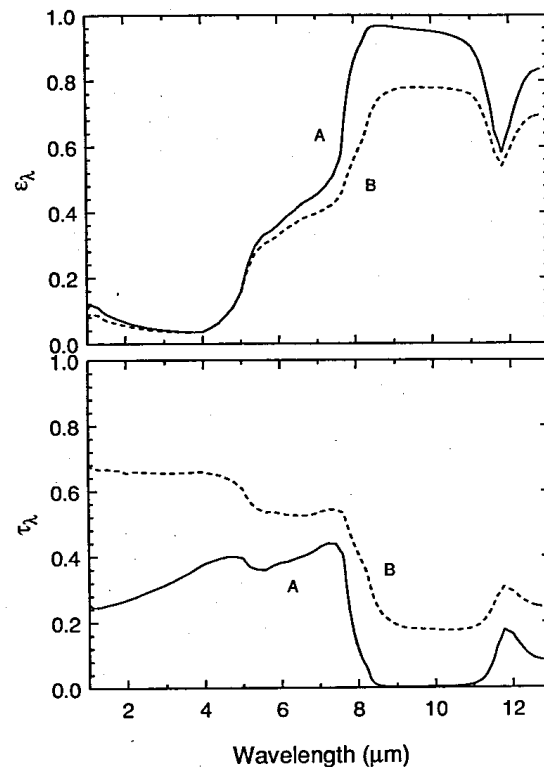

FIG. 9. Spectral hemispherical emittance and spectral diffuse transmittance for the slab containing only ash, for both size distributions A and B.

(In a more detailed treatment, the mean beam length could be corrected for finite optical depth in the gas bands, but since this correction would have to include the effects of scattering as well, it would not be straightforward. The simple approach used here is adequate for the present purposes.)

The slab spectral hemispherical emittance and diffuse transmittance are shown in Fig. 9 for flyash alone (no CO_2 or H_2O), and in Fig. 10 for the ash/CO_2/H_2O mixture. For the ash alone, the emittance is small for $\lambda < 4$ μm, and then rises rapidly at longer wavelengths, reaching a value for size distribution A of almost 1.0 near 9 μm. The emittance is greater for the finer size distribution, except near 4 μm, where the particles are only weakly absorbing. Here the emittance is independent of size distribution.

The transmittance of the slab depends strongly on particle size. For distribution A, the transmittance is low at all wavelengths. The value of the transmittance in the short wavelength region is due primarily to scattering, while the value at longer wavelengths results both from scattering and absorption. The higher transmittance for size distribution B results from lower values of the effective scattering coefficient $K'_{\lambda s}$ for this distribution, due both to the inverse dependence of the scattering coefficient on D_{32} and to the higher value of $\bar{g}_\lambda$ for this distribution. For both size distributions, the transmittance falls off significantly at longer wavelengths where, for distribution A, the layer becomes nearly opaque.

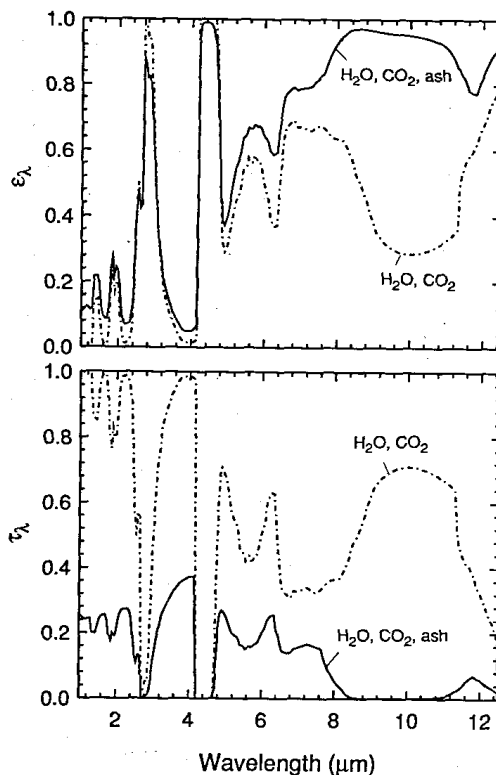The spectral emittance and transmittance of the

FIG. 10. Spectral hemispherical emittance and spectral diffuse transmittance for the slab containing CO_2, H_2O, and ash, for size distribution A.

Table 3. Total hemispherical slab emittance ε and diffuse transmittance τ for $T = 1500$ K and $T_R = 1900$ K

	Size distribution	ε	τ
CO_2, H_2O		0.2974	0.7065
Ash	A	0.1279	0.2717
	B	0.1088	0.6022
Ash, CO_2, H_2O	A	0.3531	0.1900
	B	0.3561	0.4612

ash/CO_2/H_2O mixture are shown in Fig. 10 (for distribution A only) along with the results for the CO_2/H_2O alone (no ash). For wavelengths less than 2.4 μm, both the ash and the molecular gases have fairly low emittances, and neither one dominates the combined emittance. The region from 2.4 to 4.8 μm is dominated by the strong bands of CO_2 and H_2O at 2.7 μm, and by the strong CO_2 band at 4.2 μm. The presence of the ash results in a *decrease* of the spectral emittance at the peaks of these bands, due to the ash particles scattering radiation emitted by the gases.

The largest effect of flyash on the spectral emittance occurs in the long wavelength region ($\lambda > 5$ μm). The molecular gases exhibit a region of relatively low emittance near 10 μm, where the ash has the highest emittance. At these wavelengths flyash is the dominant emitter.

As would be expected from the results in Fig. 9 for the ash alone, the presence of the ash greatly alters the transmittance of the slab, compared to the transmittance with only CO_2 and H_2O. With only the molecular combustion products present, the slab has regions of high transparency between the gas bands. With the ash, however, the transmittance is low at all wavelengths, due to scattering by the ash particles. The total hemispherical emittance and diffuse transmittance were computed from the spectral values in Figs. 9 and 10 and are tabulated in Table 3. The wavelength integration was carried out over the wavelength range from 1 to 12.5 μm. An incident radiation temperature $T_R = 1900$ K was assumed for the trans-

mittance calculations, and the computed emittance and transmittance values were normalized by the blackbody fraction in the wavelength range 1–12.5 μm (0.97 at 1500 K).

While the emittance of the CO_2/H_2O mixture alone is larger than that of the ash alone, it is clear that both are important in determining the total emittance of the gas/ash mixture, which is approximately 20% greater than that of the gas alone. It is interesting to note that while the emittance of the ash alone is lower for size distribution B than for A, in the presence of the molecular gases the situation is reversed, with the emittance of the mixture being slightly greater for distribution B than for A. This behavior is a consequence of the lower scattering coefficient for distribution B (which follows from the inverse dependence of $K'_{\lambda s}$ on D_{32} and from the greater value of $\bar{g}_\lambda$ for distribution B). Thus, the emittance in the regions of the strong gas bands is not decreased by the presence of the ash to as great an extent with size distribution B as it is with distribution A.

The emittance of the ash/gas mixture is less than the sum of the emittances of the two considered separately. This is due both to the spectral overlap of the emission of each, as well as to the scattering by the ash of radiation emitted by the gas.

The results for the total diffuse transmittance show the presence of the ash significantly reduces the layer transmittance below the value obtained when only the gases are present. This shows the significant shielding effect that a cool ash-laden layer between the flame and the wall may have, as has also been suggested previously [5].

7. SUMMARY AND CONCLUSIONS

The radiative properties of flyash and the effects of flyash on radiative heat transfer in coal combustion systems have been investigated, allowing for the first time for realistic wavelength-dependent optical constants for the flyash. The results show significant differences in comparison to previous studies, which have assumed wavelength-independent optical constants.

The radiative properties of flyash are found to be highly non-grey, which has significant implications for the contribution of flyash to heat transfer. The mean single-particle total emissivity varies between

approximately 0.05 and 0.15, depending on size distribution and temperature, and is a decreasing function of temperature. The effects of magnetite particles within the ash were examined and found to be generally small, particularly if the magnetite particles have a coarser size distribution than the glassy particles. For typical furnace conditions, flyash is predicted to increase the total emittance of the combustion products by about 20%, compared to the value calculated considering only CO_2 and H_2O. The presence of the ash in cool layers near the walls may also significantly impede the transport of hot flame radiation to the walls.

REFERENCES

1. A. Macek, Coal combustion in boilers: a mature technology facing new constraints, *Proc. Seventeenth Symp. (Int.) on Combustion*, The Combustion Institute, Pittsburgh, Pennsylvania, pp. 65–74 (1979).
2. A. F. Sarofim, Flame emissivities: alternative fuels. In *Combustion and Chemical Kinetics* (Edited by C. T. Bowman and J. Birkeland), Vol. 62 of *Progress in Aeronautics and Astronautics*. American Institute of Aeronautics and Astronautics, New York (1978).
3. A. Lowe, T. F. Wall and I. McC. Stewart, Combustion kinetics in the modeling of large, pulverized fuel furnaces: a numerical experiment in sensitivity, *A.I.Ch.E. Jl* **23**, 440–448 (1977).
4. T. F. Wall, A. Lowe, L. J. Wibberly and I. McC. Stewart, Mineral matter in coal and the thermal performance of large boilers, *Prog. Energy Combust. Sci.* **5**, 1–29 (1979).
5. T. F. Wall, A. Lowe, L. J. Wibberly, T. Mai-Viet and R. P. Gupta, Fly ash characteristics and radiative heat transfer in pulverized-coal-fired furnaces, *Combust. Sci. Technol.* **26**, 107–121 (1981).
6. R. Viskanta, A. Ungan and M. P. Mengüc, Predictions of radiative properties of pulverized coal and fly-ash polydispersions, ASME paper 81-HT-24, 20th National Heat Transfer Conf., Milwaukee, Wisconsin (April, 1981).
7. R. K. Ahluwalia and K. H. Im, Heat transfer including particle and gas radiation in subsonic MHD diffuser—II, AIAA 18th Aerospace Sciences Meeting, Pasadena, California (1980).
8. R. P. Gupta, T. F. Wall and J. S. Truelove, Radiative scatter by fly ash in pulverized-coal-fired furnaces: application of the Monte Carlo method to anisotropic scatter, *Int. J. Heat Mass Transfer* **26**, 1649–1660 (1983).
9. S. A. Boothroyd and R. A. Jones, Radiative transfer scattering data relevant to fly ash, *J. Phys. D: Appl. Phys.* **17**, 1107–1114 (1984).
10. B. A. Prentice, G. L. Fisher, C. E. Lai and T. L. Hayes, Correlation of light microscopic morphologic analysis with SEM X-ray analysis of individual coal fly ash particles, *Aerosol Sci. Technol.* **2**, 252 (1983).
11. J. B. Pollack, O. B. Toon and B. N. Khare, Optical properties of some terrestrial rocks and glasses, *Icarus* **19**, 372–389 (1973).
12. D. G. Goodwin and M. Mitchner, Optical constants of coal slags: dependence on chemical composition, *AIAA J. Thermophysics* **3**, 53–60 (1989).
13. R. Leach, Private communication.
14. D. G. Goodwin, Infrared optical constants of coal slags, Ph.D. Thesis, Stanford University, HTGL Report T-255 (1986).
15. E. R. Plante and L. P. Cook, Compositional modeling of MHD channel slag, with preliminary vapor pressure data, *Proc. 17th Symp. Engng Aspects MHD*, C.1.1–C.1.6 (1978).
16. B. Bendow, Multiphonon infrared absorption in the highly-transparent frequency regime of solids. In *Solid State Physics*, Vol. 33. Academic Press, New York (1978).
17. W. G. Driscoll (Editor), *Handbook of Optics*. McGraw-Hill, New York (1978).
18. H. Lee and R. O. Buckius, Scaling anisotropic scattering in radiation heat transfer for a planar medium, *J. Heat Transfer* **104C**, 68–75 (1982).
19. G. L. Fisher, B. A. Prentice, D. Silberman, J. M. Ondov, A. H. Bierman, R. C. Ragaini and A. R. McFarland, Physical and morphological studies of size-classified coal fly ash, *Environ. Sci. Technol.* **12**, 447–451 (1978).
20. M. S. Dobbins and G. Burnett, Production of an iron ore concentrate from the iron-rich fraction of power plant fly ash, *Res. Conserv.* **9**, 231–242 (1982).
21. C. T. Bohren and D. R. Huffman, *Absorption and Scattering of Light by Small Particles*. Wiley, New York (1983).
22. A. Schlegel, S. F. Alvarado and P. Wachter, Optical properties of magnetite (Fe_3O_4), *J. Phys. C* **12**, 1157–1163 (1979).
23. R. P. Gupta and T. F. Wall, The optical properties of fly ash in coal fired furnaces, *Combust. Flame* **61**, 145–151 (1985).
24. M. N. Özisik, *Radiative Transfer and Interactions with Conduction and Convection*. Wiley, New York (1973).
25. C. B. Ludwig, W. Malkmus, J. E. Reardon and J. A. L. Thomson, *Handbook of Infrared Radiation from Combustion Gases*, NASA SP-3080. Nat. Aero. Space Admin., Washington, DC (1973).

PROPRIETES RADIATIVES DES CENDRES VOLANTES ET EFFETS SUR LE TRANSFERT THERMIQUE RADIATIF DANS LES SYSTEMES A CHARBON INCANDESCENT

Résumé—On calcule les propriétés radiatives des polydispersions de cendres volantes, avec des constantes optiques dépendant, de façon réaliste, de la longueur d'onde. L'absorption spectrale, la diffusion et l'extinction sont présentées, en tenant compte d'un paramètre d'asymétrie de diffusion spectrale. On donne aussi les valeurs moyennes du coefficient de Planck intégrées en longueur d'onde. L'émissivité totale pour une seule particule moyenne varie entre 0,05 et 0,15 selon la distribution de taille et la température. On discute les effets des particules de magnétite, dans la cendre, sur les propriétés radiatives. La contribution de la cendre volante au transfert radiatif dans les systèmes à combustion de charbon est examinée et, pour des conditions typiques d'un foyer, la cendre volante accroît l'émittance totale d'environ 20%.

STRAHLUNGSEIGENSCHAFTEN VON FLUGASCHE UND DEREN EINFLÜSSE AUF DEN STRAHLUNGSWÄRMEAUSTAUSCH IN KOHLEBEFEUERTEN SYSTEMEN

Zusammenfassung—Unter Berücksichtigung einer realistischen Wellenlängenabhängigkeit der optischen Konstanten werden die Strahlungseigenschaften für polydisperse Flugasche berechnet. Die Koeffizienten für spektrale Absorption, Streuung und Extinktion werden gemeinsam mit dem spektralen Asymetrie-parameter der Streuung dargestellt. Außerdem werden die über die Wellenlänge integrierten Planck'schen Mittelwerte angegeben. Die mittlere Gesamtemissivität des Einzelpartikels reicht von 0,05 bis 0,15— abhängig von Größenverteilung und Temperatur. Die Einflüsse von Magnetitpartikeln in der Asche auf die Strahlungseigenschaften werden diskutiert. Der Beitrag der Flugasche zum Strahlungswärmeaustausch in kohlebefeuerten Verbrennungssystemen wird untersucht. Für typische Brennraumverhältnisse wird eine Erhöhung der Gesamtstrahlung durch die Flugasche um ungefähr 20% vorhergesagt.

РАДИАЦИОННЫЕ СВОЙСТВА ЛЕТУЧЕЙ ЗОЛЫ И ИХ ВЛИЯНИЕ НА ЛУЧИСТЫЙ ТЕПЛОПЕРЕНОС В СИСТЕМАХ СО СЖИГАНИЕМ УГЛЯ

Аннотация—Рассчитываются радиационные свойства полидисперсной летучей золы с учетом зависимости оптических постоянных от длины волны. Приведены коэффициенты спектрального поглощения, рассеяния и затухания, а также асимметричный параметр спектрального рассеяния и проинтегрированные по длине волны средние значения коэффициента Планка. Средняя величина интегральной излучательной способности одной частицы находится приближенно в диапазоне от 0,05 до 0,15 в зависимости от размера и температуры. Обсуждается влияние присутствующих в золе частиц магнетита на ее радиационные свойства. Рассматривается вклад летучей золы в лучистый теплоперенос в системах со сжиганием угля. Показано, что в типичных условиях топки летучая зола увеличивает полную излучательную способность примерно на 20%.